

NUMERICAL SIMULATION OF NANOFUID FLOW DUE TO A STRETCHABLE ROTATING DISK

Mekonnen S. Ayano, Olumuyiwa Otegbeye,
and Jochonia S. Mathunjwa

ABSTRACT. In this study, a steady magnetohydrodynamic (MHD) flow due to stretchable rotating disk in the presence of gyrotactic microorganisms is investigated. The governing equations modeling the flow are solved numerically using the newly introduced simple iteration method (SIM) that seeks to linearize a system using relaxation technique that effectively decouples the system. To verify the convergence and accuracy of the method, solution error and residual error analysis are carried out, respectively. The obtained results suggest that the SIM is a highly efficient method that produces convergent and highly accurate solutions. The effects of various parameters as well as combined parameter effects on the solution profiles are also investigated. An increase in the Hall and permeability parameters leads to a corresponding rise in the microorganism's density and nanoparticle volume fraction.

Nomenclature

u, v, w	velocity components
T	temperature
Λ	Hall parameter
D_m	diffusivity of microorganisms
C	nanoparticles volume fraction
N	local density number of the motile microorganisms
b	chemotaxis constant
Re	Reynolds number
s	constant number
M	magnetic parameter
Pr	Prandtl number
Nt	thermophoresis parameter
Nb	Brownian motion parameter
Le	Lewis number
Pe	Peclet number

2020 *Mathematics Subject Classification*: 76-11; 65L10.

Key words and phrases: stretchable rotating disk, Hall effect, porous medium, bioconvection, relaxation, spectral methods.

P	stretching parameter
Rd	radiation parameter
D_T	coefficient of thermophoretic diffusion
B_D	coefficient of Brownian diffusion
k^*	mean absorption coefficient
W_c	maximum cell swimming speed
k_1	permeability of porous medium
C_∞	concentration of nanoparticles
N_∞	concentration of the microorganisms
α	thermal diffusivity
τ	ratio of heat capacity of nanofluid and base fluid
Ω_1	angular velocity

1. Introduction

A major research focus in fluid dynamics is the improvement of the heat transfer for common fluids which mostly possess low thermal conductivity. This can be achieved by adding solid particles in these fluids. To enhance thermal conductivity in suspended nanoparticles, for example, (Au, Fe Cu) from metals and oxides, metal carbides from non-metals whose diameters are less than 100 nm of nanofluid are used. Nanofluid (nanoparticle fluid suspensions) was initially introduced by Choi [1]. Experimentally, he showed that thermal conductivity can be doubled by increasing the concentration of solid nanoparticles. Application of nanofluid can be found in several areas: medical engineering, improving transportation, microelectronics, to name a few. Buongiorno [2], in his comprehensive survey of a nanofluid model (two-phase model), investigated the significance of thermophoresis and Brownian diffusion. Several researchers studied nanofluid flow both experimentally and numerically. The first known study on stretching sheet was conducted by Khan [3] by incorporating nanofluid. In this current study, Brownian motion and thermophoresis effects were taken into consideration and it was reported that Sherwood number increases for high Prandtl number and decreases for low Prandtl number for both Brownian motion and thermophoresis parameter. The impact of Brownian motion and thermophoresis on the double-diffusive nanofluid was studied by Nield and Kuznetsov [4] who reported that an increase in the Brownian motion and thermophoresis parameters decrease the reduced Nusselt number. Silver-water nanofluid about a vertical slender cylinder was studied by Mkhatswa et al. [5] and they found that nanoparticle volume fraction and Soret number increase skin friction. Further studies on this can be found in [6–9].

Heat and mass transfer combined with nanofluid and the macroscopic movement results in the mobility of swimming microorganisms in a phenomenon known as bioconvection. The presence of gyrotactic microorganisms enhance suspension stability of nanoparticles. Some of the applications of the bioconvection phenomenon are in cancer therapy, agriculture, biotechnology, etc. Bioconvection containing nanoparticles was first studied by [10–12]. Three-dimensional rotating system with bioconvection flow of a nanofluid was studied by Shuo et al. [13] where it was

reported that the motile microorganisms flux on the wall decreases by increasing the viscosity parameter. Further studies on the impact of bioconvection have been conducted by [14–18], for example.

In industrial application, a porous medium with nanofluid is used to improve the heat transfer in processes such as water filtration, groundwater flows, fuel cells, transfer, thermal insulation, among others. Magneto-hydro-dynamic (MHD) flow with Hall currents has numerous applications in many areas such as planetary dynamics, industries, and power generators. The detailed hall phenomenon can be analysed in Chaundhary and Jain [19] paper. Due to its wide applications when the flow is in a rotating surface, several studies have investigated these areas. For MHD electrically conducting incompressible nanofluid flowing over a porous rotating disk, Rashidi et al. [20] recommended the use of the second law of thermodynamics in rotating fluid systems. Mustafa [21] reported nanoparticles volume fraction enhances the thermal layer thickness in a nanofluid flow in a rotating disk study. In non-Darcy medium three-dimensional flow due to rotating disk studied by Hayat et al. [22] showed that nanoparticles, volume fraction variation, and heat transfer rate were enhanced. Micropolar nanofluid flow between two infinite radius disks in a porous medium considering applied magnetic field was examined by Abbas et al. [23]. They showed reverse tendency related to concentration profiles with thermophoretic and Brownian motion parameters.

The main motivation of this research is to study the combined effects of radiation and Hall current effects in porous medium for bioconvective flow due to stretchable rotating disk. To the best of the authors' knowledge, the combined effect has not been studied. The partial differential equations modeling the flow transformed to nondimensional ordinary differential equation under suitable transformations. The resulting equations are solved numerically using the recently introduced simple iteration method (SIM) [24, 25], and the results are displayed graphically and in tabular form.

2. Formulation of the Problem

Consider an incompressible nanofluid flow over stretchable rotating disk. The fluid thickness is given by $z = c\left(\frac{r}{R_0} + 1\right)^{-\chi}$, it occupies the semi infinite region and the disk rotates with an angular velocity Ω_1 . (r, θ, z) coordinates are considered with the strong magnetic field parallel to the disk axis and the Hall effect retained. The temperature T_w is assumed at the surface of the disk and the ambient temperature is T_∞ . Also, it is assumed nanoparticles are not clustered together due to the stability of nanoparticles suspension. Following [22, 26] the governing equations take the form:

$$(2.1) \quad \begin{aligned} \frac{\partial u}{\partial r} + \frac{u}{r} + \frac{\partial w}{\partial z} &= 0 \\ u \frac{\partial u}{\partial r} + w \frac{\partial u}{\partial z} - \frac{v^2}{r} &= \nu \frac{\partial^2 u}{\partial z^2} - \frac{\nu}{k_1} u - \frac{\sigma B_0^2}{\rho_f(1 + \Lambda^2)} \{u + \Lambda v\} \\ u \frac{\partial v}{\partial r} + w \frac{\partial v}{\partial z} + \frac{uv}{r} &= \nu \frac{\partial^2 v}{\partial z^2} - \frac{\nu}{k_1} v + \frac{\sigma^* B_0^2}{\rho_f(1 + \Lambda^2)} \{\Lambda u - v\} \end{aligned}$$

$$\begin{aligned}
(2.2) \quad & u \frac{\partial T}{\partial r} + w \frac{\partial T}{\partial z} = \alpha_1 \frac{\partial^2 T}{\partial z^2} + \tau \left[D_B \left(\frac{\partial T}{\partial z} \frac{\partial C}{\partial z} \right) + \frac{D_T}{T_\infty} \left(\frac{\partial T}{\partial z} \right)^2 \right] + \frac{16\sigma T_\infty^3}{3k^* \rho C_p} \frac{\partial^2 T}{\partial z^2} \\
& u \frac{\partial C}{\partial r} + w \frac{\partial C}{\partial z} = D_B \frac{\partial^2 C}{\partial z^2} + \frac{D_T}{T_\infty} \left(\frac{\partial^2 T}{\partial z^2} \right) \\
& u \frac{\partial N}{\partial r} + w \frac{\partial N}{\partial z} + \frac{bW_c}{(C_w - C_\infty)} \left(\frac{\partial C}{\partial z} \frac{\partial N}{\partial z} + N \frac{\partial^2 C}{\partial z^2} \right) = D_m \frac{\partial^2 N}{\partial z^2}
\end{aligned}$$

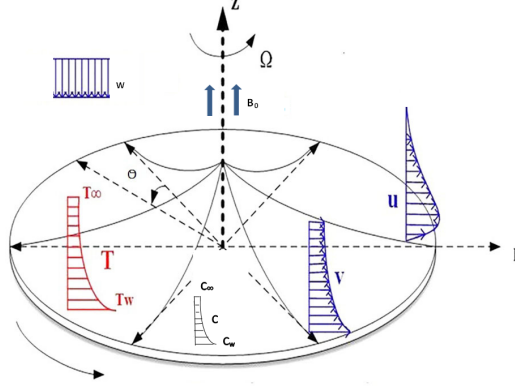


FIGURE 1. Fluid flow geometry

where C_∞, N_∞ the reference concentration of nanoparticles and reference concentration of the microorganisms, respectively. u, v, w are the velocity components of the flow, T is the temperature, Λ is Hall parameter, D_m is the diffusivity of microorganisms, C is the nanoparticles volume fraction, α_1 is the thermal diffusivity, N is the local density number of the motile microorganisms, D_T and B_D are the coefficient of thermophoretic diffusion and Brownian diffusion, k_1 is the permeability of porous medium, $\tau = \frac{(\rho c)_p}{(\rho c)_f}$ is the ratio of heat capacity of nanofluid and base fluid, σ^* is Stefan-Boltzmann constant, k^* is mean absorption coefficient, b is the chemotaxis constant, and W_c is the maximum cell swimming speed. The boundary conditions

$$\begin{aligned}
u = rc, \quad v = r\Omega_1, \quad w = 0, \quad T = T_w, \quad C = C_w, \quad N = N_w \quad \text{at } z = c \left(\frac{r}{R_0} + 1 \right)^\chi \\
u \rightarrow 0, \quad v \rightarrow 0, \quad w \rightarrow 0, \quad T = T_\infty, \quad C = C_\infty, \quad N = N_\infty \quad \text{as } z \rightarrow \infty.
\end{aligned}$$

where R_0 is the feature radius, χ is the disk thickness index and c is the thickness coefficient. Applying generalized Von Karman transformations [26]

$$\begin{aligned}
(2.3) \quad & u = r^* R_0 \Omega_1 F(\eta), \quad v = r^* R_0 \Omega_1 G(\eta), \quad \eta = \frac{z}{R_0} \left(\frac{\Omega_1 R_0^2 \rho}{\mu} \right)^{\frac{1}{n+1}}, \\
& w = R_0 \Omega_1 (1 + r^*)^s \left(\frac{\Omega_1 R_0^2 \rho}{\mu} \right)^{\frac{-1}{n+1}} H(\eta), \quad T - T_\infty = \theta (T_w - T_\infty), \\
& C - C_\infty = \phi (C_w - C_\infty), \quad N - N_\infty = \omega (N_w - N_\infty)
\end{aligned}$$

Using the transformation (2.3) on equations (2.1)–(2.2) takes the form

$$(2.4) \quad 2F + \eta\chi sF' + H' = 0$$

$$Re^{\frac{1-n}{1+n}}(1+r^*)^{2\chi}F'' - F^2 + G^2 - HF' - \eta\chi sFF' - \gamma F - \frac{M}{1+\Lambda^2}(F + \Lambda G) = 0$$

$$Re^{\frac{1-n}{1+n}}(1+r^*)^{2\chi}G'' - 2FG - HG' - \eta\chi sFG' - \gamma G + \frac{M}{1+\Lambda^2}(\Lambda F - G) = 0$$

$$Re^{\frac{1-n}{1+n}}(1+r^*)^{2\chi}[(1+Rd)\theta'' + Pr(Nb\theta' + Nt\theta'^2)] - pr(H\theta' + \eta\chi sF\theta') = 0$$

$$Re^{\frac{1-n}{1+n}}(1+r^*)^{2\chi}[\phi'' - \frac{Nt}{Nb}\theta''] - Le(H\phi' - \eta\chi sF\phi') = 0$$

$$(2.5) \quad Re^{\frac{1-n}{1+n}}(1+r^*)^{2\chi}\{\omega'' - Pe[\omega'\phi' + (\omega + \gamma_0)\phi'']\} - Lb(H\omega' + \eta\chi sF\omega') = 0$$

with boundary conditions

$$H(\alpha) = 0, \quad F(\alpha) = P, \quad G(\alpha) = 1, \quad \theta(\alpha) = 1, \quad \phi(\alpha) = 1, \quad \omega(\alpha) = 1,$$

$$F(\infty) = 0, \quad G(\infty) = 0, \quad \theta(\infty) = 0, \quad \phi(\infty) = 0, \quad \omega(\infty) = 0.$$

where $\gamma = \frac{\nu}{k_1\Omega_1}$ is the porosity parameter, $Re = \frac{\Omega_1 R_0}{\nu}$ is the Reynolds number, $s = \frac{r^*}{1+r^*}$ is a constant, $M = \frac{\sigma B_0^2}{\rho\Omega_1}$ is the magnetic parameter, $Pr = \frac{\nu}{\alpha_1}$ is the Prandtl number, $N_t = \frac{(\rho c)_p D_T(T_w - T_\infty)}{(\rho c)_f T_\infty \nu}$ is the thermophoresis parameter, $N_b = \frac{(\rho c)_p D_B(C_w - C_\infty)}{(\rho c)_f \nu}$ is the Brownian motion parameter, $Le = \frac{\nu}{D_B}$ is the Lewis number, $Pe = \frac{bW_a}{D_n}$ is the Peclet number, $P = \frac{c}{\omega_1}$ is the stretching parameter, $\alpha = \frac{c}{R_0} \left(\frac{\Omega_1 R_0^2 \rho}{\mu} \right)^{\frac{1}{n+1}}$ and $Rd = \frac{16\sigma^* T_\infty^3}{3kk^*}$ is radiation parameter.

Defining the deformation

$$(2.6) \quad H(\alpha) = h(\eta - \alpha) = h(\zeta), \quad F(\alpha) = f(\eta - \alpha) = f(\zeta), \quad G(\alpha) = g(\eta - \alpha) = g(\zeta),$$

$$\theta(\alpha) = \Theta(\eta - \alpha) = \Theta(\zeta), \quad \phi(\alpha) = \Phi(\eta - \alpha) = \Phi(\zeta), \quad \omega(\alpha) = \Omega(\eta - \alpha) = \Omega(\zeta).$$

Applying the transformation (2.6) on equations (2.4)–(2.5) we get

$$(2.7) \quad 2f + (\zeta + \alpha)\chi s f' + h' = 0$$

$$(2.8) \quad Re^{\frac{1-n}{1+n}}(1+r^*)^{2\chi}f'' - f^2 + g^2 - hf' - (\zeta + \alpha)\chi s f f' - \gamma f - \frac{M}{1+\Lambda^2}(f + \Lambda g) = 0$$

$$(2.9) \quad Re^{\frac{1-n}{1+n}}(1+r^*)^{2\chi}g'' - 2fg - hg' - (\zeta + \alpha)\chi s f g' - \gamma g + \frac{M}{1+\Lambda^2}(\Lambda f - g) = 0$$

$$Re^{\frac{1-n}{1+n}}(1+r^*)^{2\chi}[(1+Rd)\Theta'' + Pr(Nb\Theta'\Phi' + Nt\Theta'^2)] - Pr[h\Theta' + (\zeta + \alpha)\chi s f \Theta'] = 0$$

$$Re^{\frac{1-n}{1+n}}(1+r^*)^{2\chi}[\Phi'' + \frac{Nt}{Nb}\Theta''] - Le[h\Phi' + (\zeta + \alpha)\chi s f \Phi'] = 0$$

$$(2.10) \quad Re^{\frac{1-n}{1+n}}(1+r^*)^{2\chi}\{\Omega'' - Pe[\Omega'\Phi' + (\Omega + \gamma_0)\Phi'']\} - Lb[h\Omega' + (\zeta + \alpha)\chi s f \Omega'] = 0$$

with boundary conditions

$$h(0) = 0, \quad f(0) = P, \quad g(0) = 1, \quad \Theta(0) = 1, \quad \Phi(0) = 1, \quad \Omega(0) = 1,$$

$$f(\infty) = 0, \quad g(\infty) = 0, \quad \Theta(\infty) = 0, \quad \Phi(\infty) = 0, \quad \Omega(\infty) = 0.$$

where prime denotes the derivative with respect to ζ .

The shear stress in radial and tangential directions ($\tau_{zr}, \tau_{z\theta}$) and the local Nusselt number (Nu_x) respectively are

$$\begin{aligned}\tau_{zr} &= \frac{r^* \mu \Omega_1 R_0 (1 + r^*) \left(\frac{\Omega_1 R_0^2 \rho}{\mu}\right)^{\frac{1}{n+1}} f'(0)}{R_0} \\ \tau_{z\theta} &= \frac{r^* \mu \Omega_1 R_0 (1 + r^*) \left(\frac{\Omega_1 R_0^2 \rho}{\mu}\right)^{\frac{1}{n+1}} g'(0)}{R_0} \\ Nu_x &= \frac{R_0 q_w}{k(T_w - T_\infty)} \Big|_{z=0} \quad \text{where} \quad q_w \Big|_{z=0} = -k \frac{\partial T}{\partial z} + q_r \Big|_{z=0}\end{aligned}$$

The nondimensionalized skin friction, the local Nusselt number, the local wall mass flux, and the local motile microorganisms flux, respectively, are

$$C_{fx} Re^{\frac{n-1}{n+1}} = \frac{\tau_w \Big|_{z=0}}{\rho(r\Omega)^2} = \frac{1}{r^*} (1 + r^*)^\chi [(f'(0))^2 + (g'(0))^2]^{\frac{1}{2}}$$

where

$$\begin{aligned}\tau_w &= \sqrt{\tau_{zr}^2 + \tau_{z\theta}^2} \quad \text{is total shear stress,} \\ Nu_x Re^{\frac{-1}{n+1}} &= -(1 + r^*)^\chi (1 + R) \Theta'(0), \\ Sh_x Re^{\frac{-1}{n+1}} &= -(1 + r^*)^\chi (1 + R) \Phi'(0), \\ NN_x Re^{\frac{-1}{n+1}} &= -(1 + r^*)^\chi (1 + R) \Omega'(0).\end{aligned}$$

3. Numerical scheme

In this section, we apply the spectral simple iteration method (SIM) on the system of equations (2.7)–(2.10).

In the application of the simple iteration method, as expressed by Otegbeye et al. [24], the method is used in relaxing the system of equations (2.7)–(2.10) in stages. Firstly, we take equation (2.7) and linearize the nonlinear terms by setting the term with the highest order of derivative as unknown and the other term(s) as known when the nonlinear terms are in h and its derivatives. If the nonlinear terms are a mix of the function h and other functions, the other functions are set to be known irrespective of the order of derivative of h . All other terms not coupled with h are assumed to be known. Hence, relaxing equation (2.7) gives

$$(3.1) \quad h'_{r+1} = -2f_r - (\zeta + \alpha)\chi s f'_r$$

where r denotes previous time level and $r + 1$ denotes current time level. The solutions for h and its derivatives obtained in (3.1) are used in the next equation (2.8) where f and its derivatives are being solved for. In applying the same procedure described and updating solutions from previous equations, we obtain the following;

$$(3.2) \quad b_{1,r} f''_{r+1} + [b_{2,r}] f'_{r+1} + b_{3,r} f_{r+1} = b_4,$$

$$(3.3) \quad c_{1,r} g''_{r+1} + [c_{2,r}] g'_{r+1} + [c_{3,r}] g_{r+1} = c_{4,r},$$

$$(3.4) \quad d_{1,r} \theta''_{r+1} + [d_{2,r}] \theta'_{r+1} = d_{3,r},$$

$$(3.5) \quad Gr\phi''_{r+1} + [e_{1,r}]\phi'_{r+1} = e_{2,r},$$

$$(3.6) \quad Gr\Omega''_{r+1} + [f_{1,r}]\Omega'_{r+1} + [f_{2,r}] = 0,$$

where

$$\begin{aligned} Gr &= Re^{\frac{1-n}{1+n}}(1+r^{*2x}), \quad E = (\zeta + \alpha)\chi s \\ a_{1,r} &= -2f_r - Ef'_r, \quad b_{1,r} = Gr, \quad b_{2,r} = -h_{r+1} - Ef_r, \\ b_{3,r} &= -\gamma - \frac{M}{1+\Lambda^2}, \quad b_{4,r} = f_r^2 - g_r^2 + \frac{M}{1+\Lambda^2}\Lambda g_r \\ c_{1,r} &= Gr, \quad c_{2,r} = -h_{r+1} - Ef_{r+1}, \quad c_{3,r} = -2f_{r+1} - \gamma - \frac{M}{1+\Lambda^2} \\ c_{4,r} &= -\frac{M}{1+\Lambda^2}\Lambda f_{r+1}, \quad d_{1,r} = Gr(1+Rd), \quad d_{2,r} = -Prh_{r+1} - PrEf_{r+1} + PrNb\phi'_r, \\ d_{3,r} &= -PrNtGr\theta_r'^2, \quad e_{1,r} = -Leh_{r+1} - LeEf_{r+1}, \quad e_{2,r} = -\frac{Nt}{Nb}Gr\theta_{r+1}'', \\ f_{1,r} &= -Lbh_{r+1} - LbPrEf_{r+1} - PeGr\phi'_{r+1}, \quad f_{2,r} = -PeGr\phi''_{r+1}. \end{aligned}$$

The linearized decoupled system of differential equations (3.1)–(3.6) is further solved using the Chebyshev spectral method. For further knowledge on spectral methods, we refer the reader to Tang [27], Trefethen [28] and Canuto et al. [29]. This is done by transforming the semi-finite domain $\zeta \in [0, \zeta_\infty]$ to $x, y \in [-1, 1]$, respectively, where ζ_∞ is a fixed constant. The numerical solutions are defined using the Lagrange interpolation polynomials of the form

$$F(\eta, \tau) \approx \sum_{i=0}^{M_x} E(x_i) L_i(x), \quad E = h, f, g, \theta, \phi, \Omega$$

which interpolates $E(\zeta)$ at x_i where

$$x_i = \cos\left(\frac{\pi i}{M_x}\right), \quad i = 0, 1, \dots, M_x,$$

are Gauss–Lobatto collocation points. Derivatives of the unknown functions from the system of equations (3.1)–(3.6) are represented using the Chebyshev spectral method in the form

$$\left. \frac{\partial^{(m)} E}{\partial \zeta^{(m)}} \right|_{(x_i)} = \mathbf{D}^m \mathbf{E}_i, \quad m = 1, 2$$

where $\mathbf{D} = \frac{2}{\zeta_\infty} D_{l,k}$, $l, k = 0, \dots, M_x$, with $D_{l,k}$ being a differentiation matrix with dimension $(M_x + 1) \times (M_x + 1)$. \mathbf{E}_i is a vector defined as

$$\mathbf{E}_i = [E_i(x_0), E_i(x_1), \dots, E_i(x_{M_x})]^T.$$

We apply spectral methods on the decoupled system of linearized equations (3.1)–(3.6) to obtain

$$\begin{aligned} \mathbf{A}_{1,i} \mathbf{H}_{r+1,i} &= \mathbf{R}_{1,i}, & \mathbf{A}_{2,i} \mathbf{F}_{r+1,i} &= \mathbf{R}_{2,i}, & \mathbf{A}_{3,i} \mathbf{G}_{r+1,i} &= \mathbf{R}_{3,i}, \\ \mathbf{A}_{4,i} \mathbf{\Theta}_{r+1,i} &= \mathbf{R}_{4,i}, & \mathbf{A}_{5,i} \mathbf{\Phi}_{r+1,i} &= \mathbf{R}_{5,i}, & \mathbf{A}_{6,i} \mathbf{\Omega}_{r+1,i} &= \mathbf{R}_{6,i}, \end{aligned}$$

where

$$\begin{aligned}
\mathbf{A}_{1,i} &= \mathbf{D}, & \mathbf{A}_{2,i} &= [\mathbf{b}_{1,r,i}]\mathbf{D}^2 + [\mathbf{b}_{2,r,i}]\mathbf{D} + [\mathbf{b}_{3,r,i}], \\
\mathbf{A}_{3,i} &= [\mathbf{c}_{1,r,i}]\mathbf{D}^2 + [\mathbf{c}_{2,r,i}]\mathbf{D} + [\mathbf{c}_{3,r,i}], & \mathbf{A}_{4,i} &= [\mathbf{d}_{1,r,i}]\mathbf{D}^2 + [\mathbf{d}_{2,r,i}]\mathbf{D}, \\
\mathbf{A}_{5,i} &= Gr\mathbf{D}^2 + [\mathbf{e}_{1,r,i}]\mathbf{D}, & \mathbf{A}_{6,i} &= G\mathbf{D}^2 + [\mathbf{f}_{1,r,i}]\mathbf{D} + [\mathbf{f}_{2,r,i}] \\
\mathbf{R}_{1,i} &= \mathbf{a}_{1,r,i}, & \mathbf{R}_{2,i} &= \mathbf{b}_{4,r,i}, & \mathbf{R}_{3,i} &= \mathbf{c}_{4,r,i} \\
\mathbf{R}_{4,i} &= \mathbf{d}_{3,r,i}, & \mathbf{R}_{5,i} &= \mathbf{e}_{2,r,i}, & \mathbf{R}_{6,i} &= \mathbf{0}.
\end{aligned}$$

4. Results and discussion

In this section, we present the results obtained by solving the system (2.7) to (2.10). To test the convergence of the solutions and the accuracy of the approximate solutions obtained using the simple iteration method, we perform solution error and residual error analysis, respectively.

We note that, unless where varied, the results are generated using the parameter values $\chi = 1$, $\alpha = 0.3$, $Re = 0.9$, $n = 0.5$, $r^* = 0.2$, $M = 3$, $\Lambda = 2$, $p = 0.2$, $\gamma = 0.2$, $s = 0.3$, $Nt = 0.2$, $Le = 2$, $Lb = 2$, $Pe = 0.2$, $P = 0.5$, $Pr = 6.8$, $h = 0.2$, $Nb = 0.5$, and $Rd = 2$. To conduct the numerical computation, we use 30 grid points and set our semi-finite domain to a finite domain by choosing a domain $[0, 10]$ which is observed to be sufficient for obtaining consistent to 10 decimal places.

4.1. Convergence. To test the convergence of the SIM, we use the solution error which is calculated by computing the difference between solutions after successive iterations. When the error between the solutions reaches a point where further increase in iterations has no significant effect or the error is less than a very small tolerance level, we say our method converges. The solution error norms are generated thus;

$$\|\mathbf{E}\|_\infty = \max_{0 \leq i \leq M_x} \|\mathbf{E}_{r+1,i} - \mathbf{E}_{r,i}\|_\infty, \quad E = \{H, F, G, \Theta, \Phi, \Omega\}$$

Figures 2a to 2d show the solution errors of the SIM. It is observed that as the number of iterations increase, the solution error decreases linearly and it is seen that after 50 iterations, the error becomes consistent with further increase in iterations. We also observe that the error at that point is about 10^{-15} which shows that the solutions are consistent to 15 decimal places and, therefore, indicating that the SIM gives convergent solutions. As indicated, it is also observed that the solution errors decreases linearly. This is as a result of the decoupling nature of the SIM. By treating each equation independently, the solution set required involves just a function and its derivatives and hence is not affected by the solution sets of other functions.

4.2. Accuracy. To test the accuracy of the SIM, we compute the residual error by using the approximate solutions to replace the functions in the original system of equations. We use this to determine how close our solution is to the true solutions to the system of equations (2.7)–(2.10). We define the residual errors as

$$\max_{0 \leq i \leq M_t} \|\mathbf{Res}(\mathbf{E})\|_\infty \neq \mathbf{0}, \quad E = \{H, F, G, \Theta, \Phi, \Omega\}$$

It is observed from Figures 3a to 3d that the residual errors of the numerical solutions to the equations (2.7)–(2.9) and (2.10) gets smaller as the number of iterations increase until an error of 10^{-15} is obtained. The error remains consistent as the number of iterations are further increased. From the figures, we see that the SIM gives highly accurate solutions as evidenced by the error obtained.

TABLE 1. Skin friction, local Nusselt number, local wall mass flux, and local wall motile microorganisms flux

$\frac{1}{r^*}(1+r^*)^\chi((f'(0))^2+(g'(0))^2)^{\frac{1}{2}}$	7.3395133615495443
$-(1+r^*)^\chi(1+Re)\theta'(0)$	0.0180572801736315
$-(1+r^*)^\chi(1+Re)\phi'(0)$	0.4093352349899516
$-(1+r^*)^\chi(1+Re)\Omega'(0)$	0.2439886928064788

Having established the convergence and accuracy of the solutions obtained using the SIM, we investigate the effect of certain parameters on the various solution profiles. To achieve convergence of solutions displayed in Table 1 to 16 decimal places, we need 36 iterations.

Finally, the present results are validated with those obtained in Xun et al. [30] and Ming et al. [31] and found in an excellent agreement as depicted in Table 2.

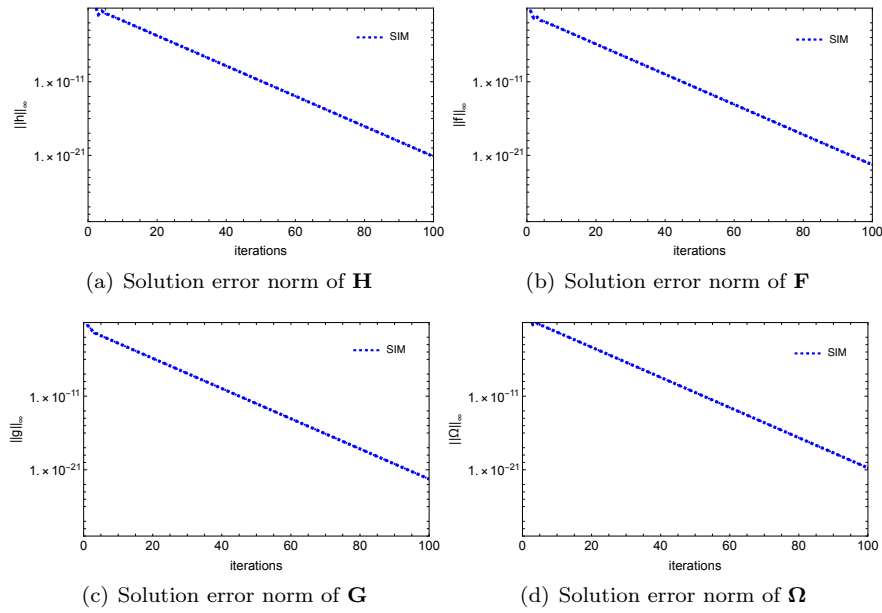


FIGURE 2. Effect of iterations on the solution error norms

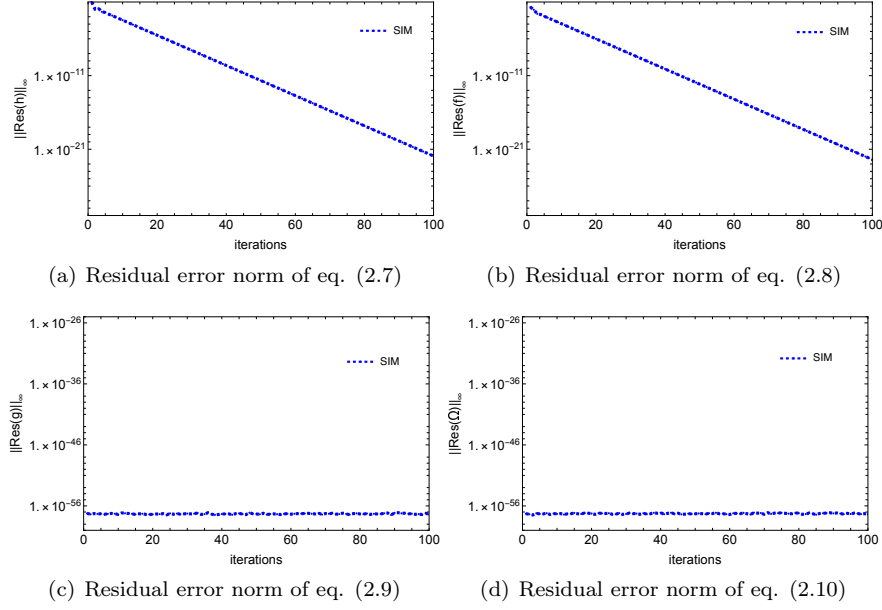


FIGURE 3. Effect of iterations on the residual error norms when $\xi = 4$

TABLE 2. Validation of the present values $f'(0)$, $g'(0)$ and $\theta'(0)$ when $\chi = \alpha = r^* = Nt = Lb = Le = Rd = 0$, $\alpha = 0.8$, $Re = 0.9$, $n = 1$, $s = 0.8$, $Pr = 1$

Authors	$f'(0)$	$-g'(0)$	$-\theta'(0)$
Present	0.51023	0.61592	0.39625
Xun et al. [30]	0.510231	0.615921	0.396271
Ming et al. [31]	0.51021	0.61591	0.39632

Figures 4(a–d) display the effect of the stretching parameter on the skin friction, local Nusselt number, local mass flux, and local wall motile microorganisms flux. The wall shear stress is described as the fluid flowing over the surface of the stretchable rotating disk. The wall shear stress is enhanced with an enhancement of the stretching parameter. It is observed that the Nusselt number increases near the boundaries with an increase in the stretching parameter, but it leads to a decrease in the mass and motile microorganisms for $0 \leq \zeta \leq 4$.

4.3. The effect of radiation, thermophoresis and Brownian motion parameters. Figures 5(a–d) display that the temperature and concentration profiles are increased with an increase of the thermophoresis and Brownian motion parameters. The thermophoretic force in fluids move fluid particles from regions

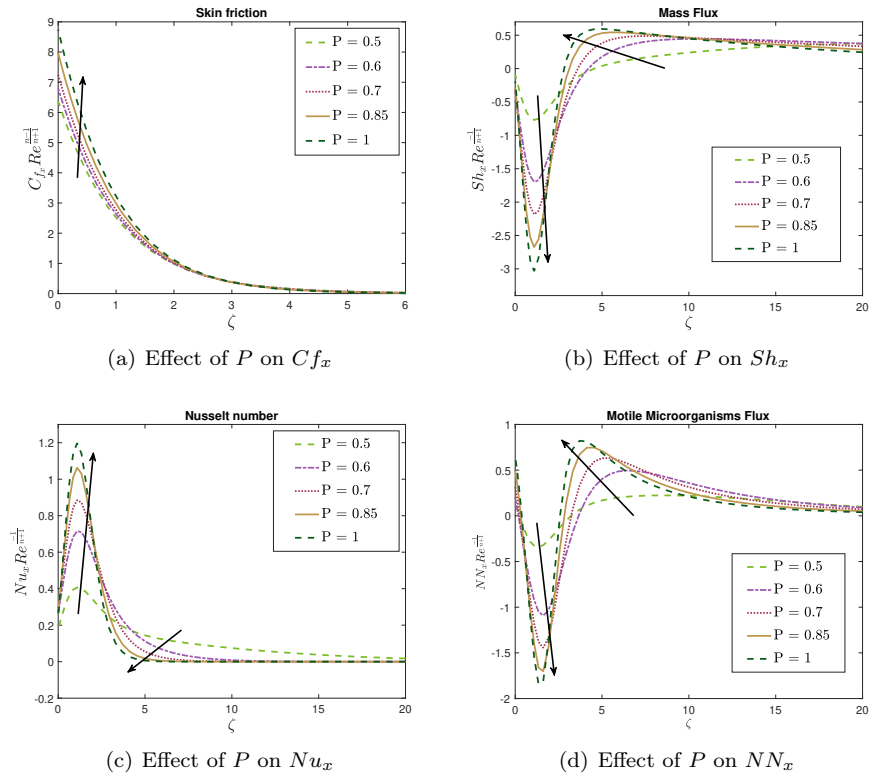
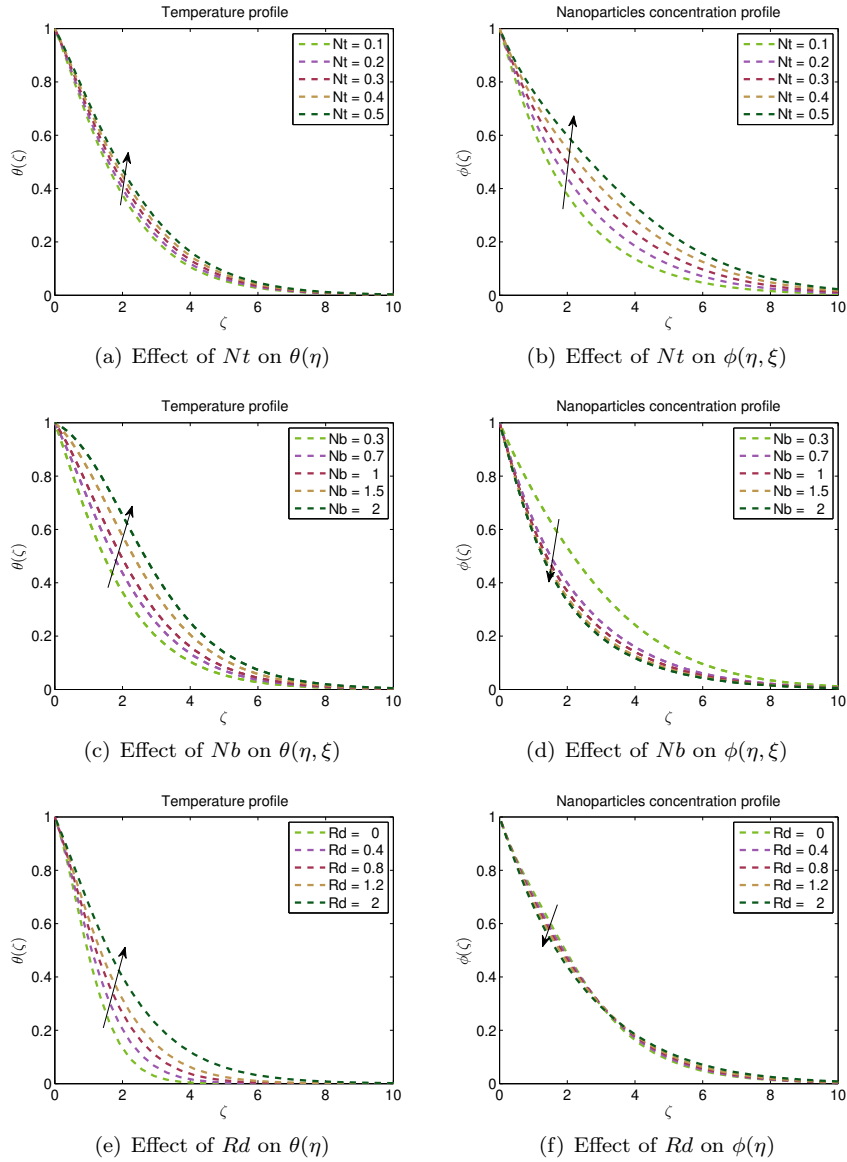


FIGURE 4. Effect of stretching parameter (P) on the skin friction, mass flux, Nusselt number, and motile microorganism flux.

of hot surface to low and thus the volume fraction distribution boosts. Hence, the rises in the temperature and concentration are gradual enhancement in nanoparticles percentage with thermophoresis. Random motion or Brownian motion of nanoparticles also shows important movement of nanoparticles; it describes the ratio of nanoparticle diffusion to the thermal diffusion in the nanofluid through Brownian motion parameter. Increasing the value of the random movement, and also the colliding of macroscopic particles the temperature of the fluid increases from Figure 5(c). However, the concentration decreases with the increase of the Brownian motion parameter in Figure 5(d). The influence of thermal radiation parameter on the fluid temperature and concentration is shown in Figures 5(e-f). The radiation parameter describes the relative contribution of conduction heat transfer to thermal radiation transfer. It is found that the temperature of the fluid increases with the increase in the value of the radiation parameter in Figure 5(e). This is because of a decrease in the Rosseland radiation absorptivity as the radiation parameter increases. The opposite effect is observed for concentration as seen in Figure 5(f).

FIGURE 5. Effect of Nt , Nb and Rd

4.4. The effect of Hall parameter. Figures 6(a–e) show the effects of Hall current parameter on the flow. It is observed in Figures 6(a) and 6(c) that, as the Hall parameter ($\Lambda \leq 1$) increases, the velocity profiles increase. This is because the reducing effect of the magnetic field due to the damping effect is enhanced by inducing secondary flow, g , and this process decreases the primary flow, as shown

in Figure 6(b). The temperature increases with the increase in the Hall parameter as seen in Figures 6(d). The magnetic force increases friction between the fluid and disk surface resulting in an increase in temperature of the fluid. A similar effect is observed in the concentration and gyrotactic microorganism concentration from Figures 6(e–f).

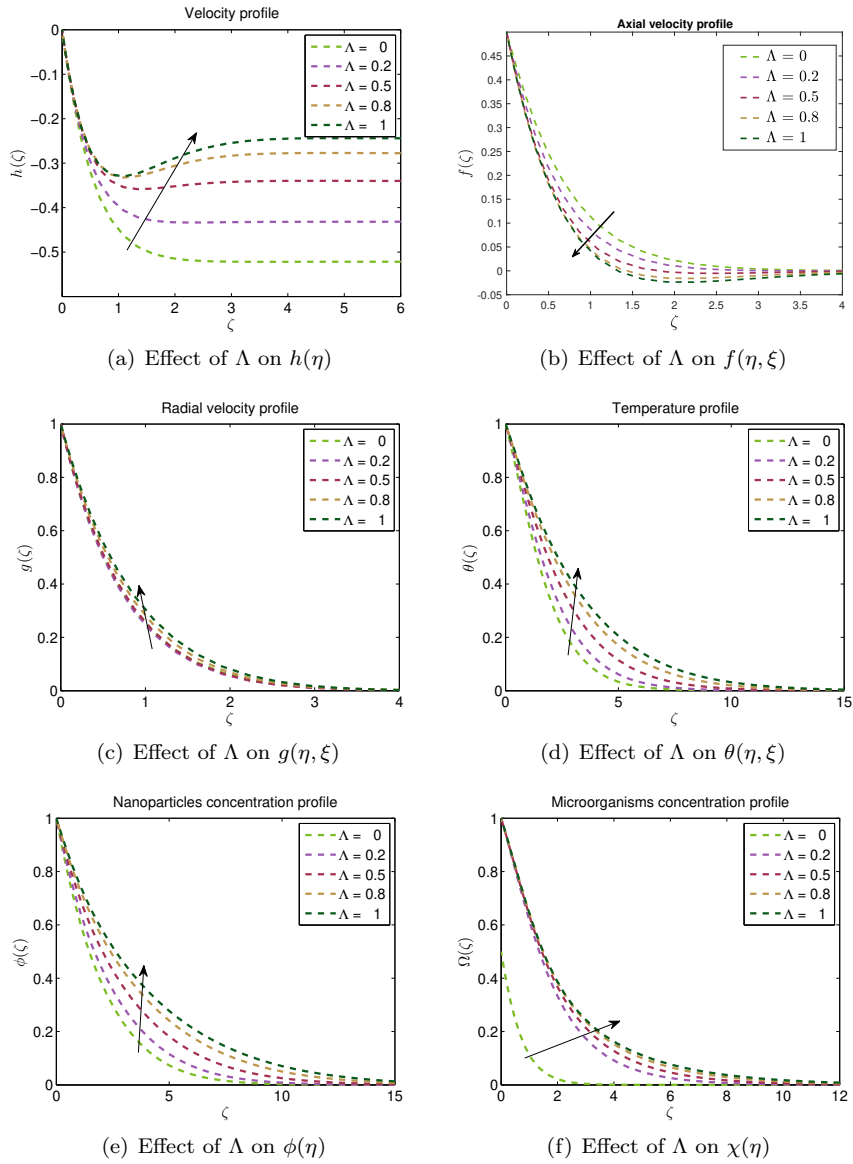
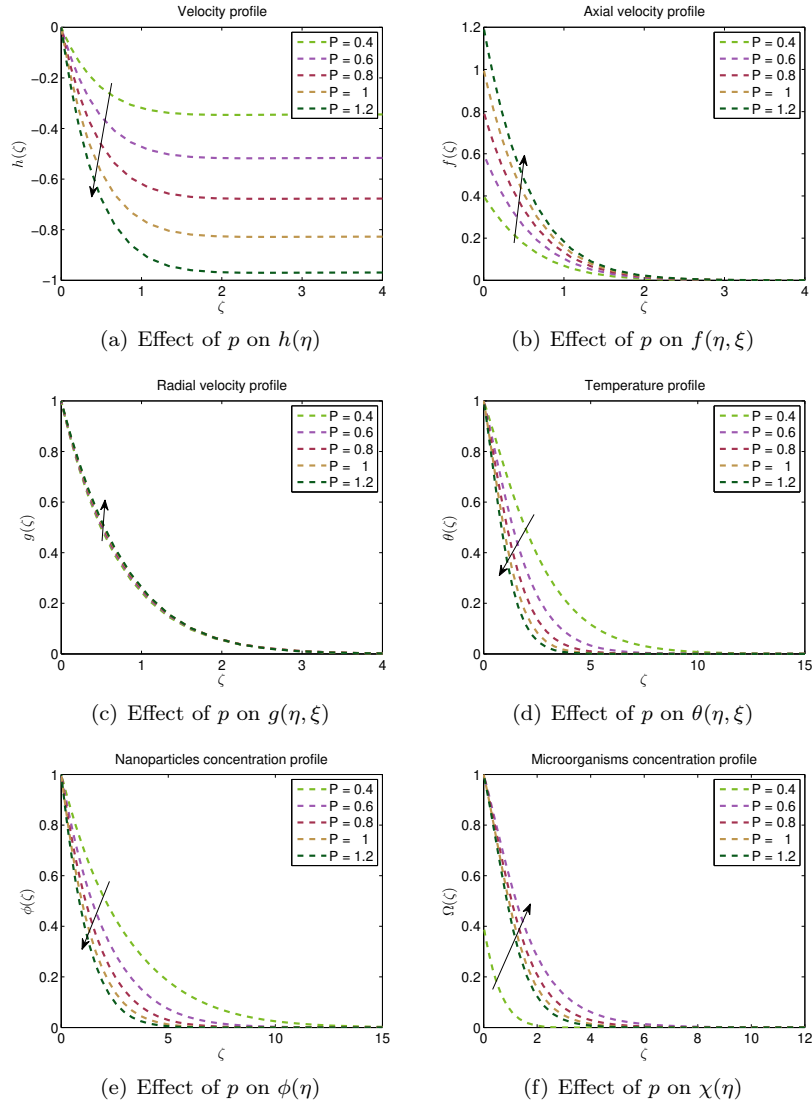


FIGURE 6. Effect of Hall parameter Λ

FIGURE 7. Effect of stretching parameter p

4.5. The effect of stretching parameter. The impact of stretching parameter on velocities is presented in Figures 7(a–c). The radial and tangential velocities increases with the increase of stretching parameter. A similar observation in magnitude is seen for the axial velocity. Negative values in the axial velocity show that the flow is in the reverse direction. Gyrotactic microorganism concentration falls when stretching parameter is increased, but the temperature and concentration increase with increases in the values of stretching parameter as seen in Figures 7(d–f).

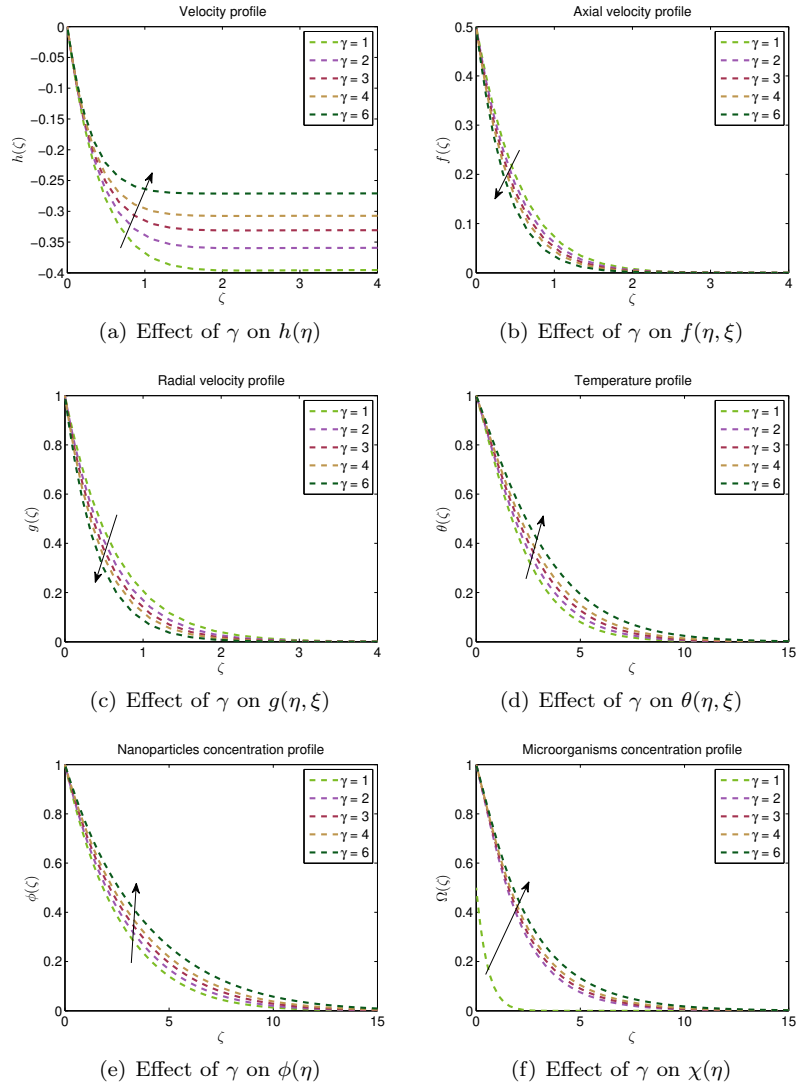


FIGURE 8. Effect of permeability parameter γ

4.6. The effect of permeability parameter. Figures 8(a–c) show the effect of permeability parameter of porous medium. The increase of permeability parameter results in the decrease of the flow velocity. The more the medium is porous, the higher the restriction is to the fluid flow which causes deceleration of the motion. It is observed in Figure 8(d) that porosity parameters increase shows an increase in temperature, as a result of the increase in the boundary layer caused by viscosity. A similar relation shows in the profile of concentration and gyrotactic microorganism concentration in Figures 8(e–f).

5. Conclusion

In this study, the flow over stretchable disks under the influence of magnetic field was investigated. Numerical analysis was carried out using the simple iteration method (SIM). The accuracy and convergence of the solutions obtained using the SIM were established by analysis and matching results from literature. The effects of porosity, Hall, radiation, Brownian motion, and thermophoresis parameters were studied. The key conclusions are:

- The more the disk is stretched the profile of the temperature decreases.
- An increase in the permeability parameter causes an increase in the surface temperature.
- The increase in the Hall parameter increases the radial and tangential velocities while decreasing the radial velocity.
- Thermophoresis parameter increase enhances the temperature and concentration.
- The increase in Brownian motion parameter decreases the concentration.

References

1. S. U. S. Choi, *Enhancing conductivity of fluids with nanoparticles*, ASME Fluid Eng. Division **231** (1995), 99–105.
2. J. Buongiorno, *Convective transport in nanofluids*, J. Heat Transfer **128**(3) (2006), 240–250.
3. W. A. Khan, I. Pop, *Boundary-layer flow of a nanofluid past a stretching sheet*, Int. J. Heat Mass Transfer **53**(11–12) (2010), 2477–2483.
4. D. A. Nield, A. V. Kuznetsov, *The Cheng-Minkowycz problem for the double-diffusive natural convective boundary layer flow in a porous medium saturated by a nanofluid*, Int. J. Heat Mass Transfer **54**(1–3) (2011), 374–378.
5. M. P. Mkhathshwa, S. S. Motsa, M. S. Ayano, P. Sibanda, *MHD mixed convective nanofluid flow about a vertical slender cylinder using overlapping multi-domain spectral collocation approach*, Case Stud. Therm. Eng. **18** (2020), 100598.
6. O. D. Makinde, A. Aziz, *Boundary layer flow of a nanofluid past a stretching sheet with a convective boundary condition*, Int. J. Therm. Sci. **50**(7) (2011), 1326–1332.
7. J. Raza, F. Mebarek-Oudina, A. Chamkha, *Magnetohydrodynamic flow of molybdenum disulfide nanofluid in a channel with shape effects*, Multidiscip. Model. Mater. Struct. **15**(4) (2019), 737–757.
8. M. Mesbah, A. Vatani, M. Siavashi, M. H. Doranehgard, *Parallel processing of numerical simulation of two-phase flow in fractured reservoirs considering the effect of natural flow barriers using the streamline simulation method*, Int. J. Heat Mass Transfer **131** (2019), 574–83.
9. A. A. Afify, M. A. A. Bazid, *Effects of variable fluid properties on the natural convective boundary layer flow of a nanofluid past a vertical plate: Numerical study*, J. Comput. Theor. Nanosci. **11**(1) (2014), 210–218.
10. A. V. Kuznetsov, A. V. Avramenko, *Effect of small particles on the stability of bioconvection in a suspension of gyrotactic microorganisms in a layer of finite depth*, Int. Commun. Heat Mass Transfer **31**(1) (2004), 38.
11. P. Geng, A. V. Kuznetsov, *Effect of small solid particles on the development of bioconvection plumes*, Int. Commun. Heat Mass Transfer **31** (2004), 629.
12. P. Geng, A. V. Kuznetsov, *Settling of bidispersed small solid particles in a dilute suspension containing gyrotactic micro-organisms*, Int. J. Eng. Sci. **43** (2005), 992.

13. X. Shuo, Z. Jinhu, Z. Liancun, Z. Xinxin, *Bioconvection in rotating system immersed in nanofluid with temperature dependent viscosity and thermal conductivity*, Int. J. Heat Mass Transfer **111** (2017), 1001–1006.
14. W. A. Khan, O. D. Makinde, Z. H. Khan, *MHD boundary layer flow of a nanofluid containing gyrotactic microorganisms past a vertical plate with Navier slip*, Int. J. Heat Mass Transfer **74** (2014), 285–291.
15. S. E. Ahmed, H. F. Oztop, M. A. Mansour, N. Abu-Hamdeh, *MHD mixed thermo-bioconvection in porous cavity filled by oxytactic microorganisms*, Therm. Sci. **22**(6B) (2018), 2711–2721.
16. C. S. Balla, C. Haritha, N. Kishan, A. M. Rashad, *Bioconvection in nanofluid-saturated porous square cavity containing oxytactic microorganisms*, Int. J. Numer. Methods Heat Fluid Flow **29**(4) (2019), 1448–1465.
17. S. A. Mekonnen, *Comparative analysis MHD biocovective flow of micropolar nanofluid in a porous medium*, Int. J. Heat Technol. **39**(3) (2021), 727–736.
18. P. B. S. Kumar, B. J. Gireesha, B. Mahanthesh, A. J. Chamkha, *Thermal analysis of nanofluid flow containing gyrotactic microorganisms in bioconvection and second-order slip with convective condition*, J. Therm. Anal. Calorim. **136**(5) (2019), 1947–1957.
19. R. C. Chaudhary, P. Jain, *Hall effect on MHD mixed convection flow of a viscoelastic fluid past an infinite vertical porous plate with mass transfer and radiation*, Ukr. J. Phys. **52** (2007), 10.
20. M. M. Rashidi, S. Abelman, M. N. Freidooni, *Entropy generation in steady MHD flow due to a rotating porous disk in a nanofluid*, Int. J. Heat Mass Transfer **62** (2013), 515–525.
21. M. Mustafa, *Cattaneo–Christov heat flux model for rotating flow and heat transfer of upper-convected Maxwell fluid*, AIP Adv. **5**(4) (2015), 047109.
22. T. Hayat, T. Nasir, M. I. Khan, A. Alsaedi, *Non-Darcy flow of water-based single (SWCNTs) and multiple (MWCNTs) walls carbon nanotubes with multiple slipconditions due to rotating disk*, Results Phys. **9** (2018), 390–399.
23. Z. Abbas, T. Mushtaq, S. A. Shehzad, A. Rauf, R. Kumar, *Slip flow of hydromagnetic micropolar nanofluid between two disks with characterization of porous medium*, J. Braz. Soc. Mech. **41** (2019), 465.
24. O. Otegbeye, Md. S. Ansari, T. P. Singh, M. Trivedi, S. P. Goqo, *Unsteady flow of Jeffrey nanofluid: A numerical simulation by bivariate simple iteration method*, Adv. Appl. Math. Sci. **19**(12) (2020), 1279–1307.
25. O. Otegbeye, M. S. Ansari, *A finite differencebased simple iteration method for solving boundary layer flow problems*, AIP Conf. Proc. **2435**(1) (2022), 020055.
26. T. Hayat, S. Qayyum, M. Imtiaz, M. Alsaedi, *Radiative flow due to stretchable rotating disk with variable thickness*, Results Phys. **7** (2017), 156–165.
27. T. Tang, *Spectral and high-order methods with applications*, Science press, Beijing, 2006.
28. L. N. Trefethen, *Spectral Methods in MATLAB*, SIAM, Philadelphia, 2000.
29. C. Canuto, M. Y. Hussieni, A. Quarteroni, T. A. Zang, *Spectral Methods in Fluid Dynamics*, Springer-Verlag, Berlin, 1988.
30. S. Xun, J. Zhao, L. Zheng, X. Chen, X. Zhang, *Flow and heat transfer of Ostwald-deWaele fluid over a variable thickness rotating disk with index decreasing*, Int. J. Heat Mass Transfer **103** (2016), 1214–24.
31. C. Y. Ming, L. C. Zheng, X. X. Zhang, *Steady flow and heat transfer of the powerlaw fluid over a rotating disk*, Int. Commun. Heat Mass Transfer **38** (2011), 280–284.

НУМЕРИЧКА СИМУЛАЦИЈА ТОКА НАНОФЛУИДА ИЗНАД РОТИРАЈУЋЕГ ДИСКА

РЕЗИМЕ. У овој студији истражује се стационаран магнетохидродинамички (МНД) ток изнад ротационог диска у присуству гиротактичких микроорганизама. Једначине које моделирају ток се решавају нумерички користећи новоуведену методу једноставне итерације (SIM) која настоји да линеаризује систем користећи технику релаксације која ефикасно раздваја систем. Да би се проверила конвергенција и тачност методе, врши се анализа грешке решења и заосталих грешака. Добијени резултати сугеришу да је SIM веома ефикасан метод који даје конвергентна и високо прецизна решења. Такође се истражују ефекти различитих параметара, као и комбиновани утицаји параметара на профиле раствора. Повећање Холовог параметара и пермеабилности доводи до одговарајућег пораста густине микроорганизама и запреминског удела наночестица.

Department of Mathematics
University of Eswatini
Eswatini
mekk_aya@yahoo.com

(Received 10.08.2022)
(Revised 06.04.2023)
(Available online 17.05.2023)

School of Computer Science and Applied Mathematics
University of the Witwatersrand
South Africa
muyiwabowen@gmail.com

Department of Mathematics
University of Eswatini
Eswatini
jsmaths@uniswa.sz